SUPPLEMENTARY MATERIAL

Evidence for a Long Period Compressibility Limit

As noted in the main text, Yamamoto (1982) presents a detailed derivation of the compressibility limit for a hydrostatic water column. Physically, the compressibility limit occurs because the water column is not welded to the seafloor and is confined only by hydrostatic pressure. As the wavelength of an upward propagating acoustic wave exceeds the shallow water limit ($\lambda > 4H$), the hydrostatic pressure of the water column ceases to provide enough confining pressure to support compression throughout the entire vertical deviation from elastic equilibrium (i.e., $\lambda/4$). Vertical motion is not lost, however, but is instead accommodated as a bulk (incompressible) displacement governed by gravity rather than elasticity. Partial compression will still occur near the seafloor but will decrease exponentially with upward vertical distance (i.e., an evanescent wavefield). Note that the cutoff effect is not directionally symmetric: for a downward-directed acoustic source near the surface of the water column, the confining pressure is supplied by the structural rigidity of the Earth and is therefore functionally infinite. Any upwards reflected elastic energy from the seafloor will decay evanescently, however.

We define an incompressible medium as having constant density ($\frac{\delta\rho}{\delta t} = 0$) at all volumetric scales. The velocity of longitudinal stress fields, $c_L = \sqrt{\frac{\Lambda+2\mu}{\rho}}$, is infinite for an incompressible medium, where Λ is the first Lamé parameter and μ is the shear modulus. The velocity of compressional waves, $\alpha = \lambda f$, is undefined as a direct consequence of the time-invariant density: the amplitude of a compressional wave in an incompressible medium is zero, so the wave equation is also zero at all times.

We present observations that we interpret as evidence for acoustic cutoff behavior. We will use floating station RS16 (Figures 3, S5) and grounded station RS08 (Figures 4, S6) as references; however, these observations are valid for any floating or grounded station from the RIS/DRIS experiment.

1. For the event shown in Figure 3, at RS16:
   (a) P-waves arrive with a ray parameter of 0.06 s km^{-1}, or angles of incidence of 4.5° in the water and 12.4° in the ice.
   (b) S-waves arrive with a ray parameter of 0.11 s km^{-1}. Scattered P-waves would have angles of incidence of 9.0° in the water and 24.8° in the ice.
   (c) Both ray parameters are well below the water/ice critical angle of 22.4° (0.26 s/km) (Figure S3).
   (d) The acoustic cutoff period, as estimated with Equation 4, is $P_c \approx 2.0$ s.
2. P-wave arrivals with periods less than 3 s are observed strongly on all three channels at both floating and grounded stations. Notably, the SNR across all three channels is generally self-similar at RS16 and RS08.
   (a) Because there are no S-waves in the water, all horizontal power observed at RS16 must be the result of P-to-S conversions at the ice/water and ice/free surface boundaries.
   (b) The wintertime horizontal background noise is generally at the New Low Noise Model (NLNM) in the 0.4–4.0 s band (Baker and others, 2019). This helps the SNR of the horizontal scattered signal, considering that scattering coefficients are on the order of only 5% (Figure S3).
   (c) Horizontal component signal with periods of 2–3 s (i.e., greater than the estimated acoustic cutoff) may be the result of evanescent tunneling.
3. P-wave arrivals with periods greater than 10 s are observed on all three channels at RS08; Z and R are stronger than T, as expected for P-waves. In contrast, at RS16, these same long period P-waves are observed only on the vertical channel.

(a) Teleseismic P-waves generate significant scattered S-waves in the ice, as shown by the horizontal signal at periods less than 3 s. For a fully elastic ice shelf, P-waves incident on the water/ice interface should generate S-waves in the ice for all angles of incidence greater than normal.

(b) By the working theory, 10–20 s P-wave arrivals are above the acoustic cutoff period and therefore would not excite acoustic waves in the water column. In other words, in response to the displacement of the seafloor by the solid Earth P-wave, the water column responds as an incompressible mass and all physics governing elastic wave propagation are irrelevant. Such incompressible displacement of the water/ice column would only register on the seismometer as a vertical displacement (since again, there are no elastic waves in the water column at these periods to scatter into horizontal power). This is consistent with what we observe at floating stations.

(c) Wintertime horizontal noise in the 10–20 s band is also very nearly at the NLNM. Coincidentally, the absolute power of the NLNM is similar in the 0.4–4.0 s and 10–20 s bands. Stronger noise can therefore be ruled out as the cause of the lack of horizontal power coincident with the 10–20 s P-wave arrivals.

4. Teleseismic S-wave arrivals (10–15 s) are strongly observed on all three channels at RS08 (grounded), consistent with basic theory.

(a) S-to-P wave conversions can occur at the Moho, the sediment/basement interface, and the seafloor/water interface. Following classical elastic theory, at RS16, we would predict to observe vertical signal resulting from teleseismic S-to-P conversions at the aforementioned interfaces, as well as horizontal signal resulting from P-to-S scattering at the ice/water interface and the ice free surface. Additionally, due to the steeper angles of incidence for teleseismic S-waves, these conversions should produce ∼2x more scattered energy in the ice layer relative to the teleseismic P-waves.

(b) Seafloor sediments would create strong S-wave resonances which would continually leak additional acoustic wave energy into the water column, to be scattered into P- and S-waves in the ice layer. For a fully elastic water/ice column, the observed P- and S-wave budget would be substantial. In reality, we see only vertical signal at periods longer than 10 s (with the exception of horizontal signal that can be attributed to Lamb waves, as described in the main text).

(c) Vertical SNR in the 10–15 s band at RS16 is ∼30 dB. For P-wave arrivals with periods shorter than 3.0, 30 dB of SNR on the vertical channel resulted in observable signal on the horizontal channels. Noise levels between the two bands are similar, so a direct comparison of SNR is valid. The conclusion, again, is that short period displacement of the seafloor generates elastic waves in the water/ice column, while long period displacement generates incompressible waves governed by gravity.

(d) Horizontal noise at periods greater than 20 s is at the New High Noise Model (NHNM). At these long periods, the lack of horizontal signal could be attributed to high noise. However, by the presented logic, we do not expect to see any signal.

5. Rayleigh waves follow a similar pattern.

(a) Rayleigh waves should be leaky for the seafloor/water interface and would radiate P-wave energy at a characteristic angle (26.5°). These water column P-waves would be post-critical at the water/ice interface and would convert 80% of their energy into SV-waves in the ice. Consistent with this, we do observe some radial power at RS16 coincident with the peak (> 50 dB) Rayleigh wave power, beginning around 2500 s. This may also be evanescent tunneling of elastic energy across the water column, which may scatter into S-wave energy in the ice. Whether this radial power is the entirety of the expected power, or is actually due to evanescent tunneling, is unclear at this time.

Supplementary Tables

Table S1. Comparative measurements of Ross Ice Shelf total ice thickness ("Ice"), subshelf cavity thickness ("H_2O"), and orthometric elevation ("Elv") for all floating stations. The GPS column lists the averaged coordinates for the entire deployment period, derived from twice-daily telemetered state-of-health reports. The "PSD" column shows ice and water layer thicknesses as derived with Equation (3), Table 2, and resonance periods manually selected from the median P-wave arrival PSDs (e.g., Fig. 6). Data from ROSETTA, BedMachine, and BEDMAP2 were bicubicly interpolated to the listed GPS coordinates; surface elevations are referenced to the EIGEN-6C4 geoid (Morlighem and others, 2020). BedMachine and BEDMAP2 use an outdated coastline mask for the RIS and consequently do not include ice shelf measurements for the current location of the ice front (i.e., DR01–DR03). ROSETTA has data gaps in bathymetry at DR02 and surface elevation for DR01–DR03; for the latter, we instead list the orthometric elevations as determined by hydrostatic buoyancy. All ice thicknesses and elevations include the firn layer. All values are in kilometers, for consistency with Tables 1 and 2.

	GPS		PSD			ROSETTA			BedMachine			BEDMAP2		
Station	Lat	Lon	Ice	H_2O	Elv	Ice	H_2O	Elv	Ice	H_2O	Elv	Ice	H_2O	Elv
DR01	−77.767	178.346	0.212	0.489	0.039	0.237	0.466	0.041		0.684			0.745	
DR02	−77.824	−178.424	0.169	0.532*	0.034	0.115		0.028		0.634			0.690	
DR03	−78.262	−175.115	0.220	0.316	0.040	0.241	0.299	0.042		0.500			0.598	
DR04	−78.280	−178.794	0.293	0.481	0.047	0.227	0.467	0.036	0.253	0.466	0.045	0.272	0.498	0.043
DR05	−78.632	−179.093	0.306	0.420	0.049	0.207	0.485	0.046	0.306	0.426	0.048	0.295	0.471	0.046
DR06	−78.788	−179.715	0.320	0.458	0.050	0.318	0.411	0.044	0.310	0.453	0.051	0.317	0.470	0.049
DR07	−78.931	179.198	0.300	0.523	0.048	0.295	0.468	0.051	0.295	0.480	0.048	0.307	0.508	0.047
DR08	−78.949	179.658	0.332	0.481	0.052	0.313	0.442	0.050	0.316	0.465	0.050	0.312	0.504	0.049
DR09	−78.957	179.889	0.311	0.426	0.049	0.310	0.430	0.048	0.329	0.446	0.051	0.321	0.490	0.050
DR10	−78.965	−179.880	0.323	0.458	0.051	0.324	0.416	0.051	0.338	0.434	0.051	0.330	0.473	0.051
DR11	−78.996	−178.953	0.326	0.359	0.051	0.338	0.380	0.049	0.356	0.401	0.051	0.323	0.423	0.050
DR12	−79.009	−179.922	0.329	0.489	0.051	0.320	0.423	0.047	0.331	0.451	0.050	0.327	0.479	0.051
DR13	−79.054	−179.965	0.320	0.458	0.050	0.290	0.462	0.045	0.333	0.458	0.049	0.329	0.478	0.050
DR14	−79.142	179.948	0.326	0.466	0.051	0.316	0.453	0.044	0.378	0.431	0.048	0.327	0.468	0.050
DR15	−79.492	−179.920	0.320	0.432	0.050	0.301	0.422	0.047	0.357	0.409	0.048	0.350	0.426	0.053
DR16	−80.869	178.431	0.348	0.317	0.053	0.336	0.240	0.053	0.336	0.278	0.053	0.351	0.286	0.052
RS01	−78.184	169.965	0.286	0.685*	0.047	0.255	0.566	0.030	0.252	0.598	0.041	0.222	0.703	0.040
RS02	−78.493	173.346	0.332	0.523	0.052	0.333	0.492	0.051	0.346	0.509	0.051	0.326	0.544	0.050
RS03	−78.760	176.878	0.314	0.426	0.050	0.322	0.328	0.047	0.283	0.392	0.051	0.325	0.379	0.050
RS04	−78.981	−179.418	0.320	0.414	0.050	0.353	0.387	0.055	0.330	0.446	0.048	0.319	0.460	0.050
RS05	−79.160	−175.533	0.317	0.286	0.050	0.328	0.255	0.049	0.329	0.290	0.052	0.330	0.293	0.051
RS06	−79.283	−171.620	0.332	0.335	0.052	0.349	0.353	0.047	0.347	0.389	0.053	0.342	0.344	0.052
RS07	−79.365	−167.605	0.386	0.226	0.058	0.402	0.186	0.042	0.408	0.245	0.060	0.405	0.221	0.059
RS10	−79.279	−155.469	0.593*	0.187	0.080	0.586	0.100	0.075	0.588	0.164	0.082	0.616	0.179	0.080
RS15	−80.496	−169.979	0.378	0.089	0.057	0.378	0.051	0.046	0.397	0.085	0.055	0.375	0.099	0.054
RS16	−80.133	179.368	0.311	0.397	0.049	0.308	0.354	0.045	0.304	0.401	0.049	0.312	0.421	0.049
RS18	−81.594	177.335	0.359	0.221	0.055	0.370	0.198	0.052	0.344	0.259	0.055	0.369	0.238	0.054
Median			0.320	0.426	0.050	0.318	0.414	0.047	0.332	0.429	0.051	0.327	0.464	0.050
MAD			0.012	0.063	0.002	0.023	0.057	0.003	0.023	0.037	0.002	0.015	0.042	0.001

* Both the $n = 1$ and $n = 2$ resonance harmonics were identified for these layers at these locations. For all other locations, only the $n = 1$ harmonic could be identified.

Table S2. Residuals between the current study (PSD) and the supplemental datasets for the values listed in Table S1

	PSD - ROSETTA			PSD - BedMachine			PSD - BEDMAP2		
Station	Ice	H_2O	Elv	Ice	H_2O	Elv	Ice	H_2O	Elv
DR01	−0.025	0.023	−0.002						
DR02	0.054		0.006						
DR03	−0.021	0.017	−0.002						
DR04	0.066	0.014	0.011	0.040	0.015	0.002	0.021	−0.017	0.004
DR05	0.099	−0.065	0.003	0.000	−0.006	0.001	0.011	−0.051	0.003
DR06	0.002	0.047	0.006	0.010	0.005	−0.001	0.003	−0.012	0.001
DR07	0.005	0.055	−0.003	0.005	0.043	0.000	−0.007	0.015	0.001
DR08	0.019	0.039	0.002	0.016	0.016	0.002	0.020	−0.023	0.003
DR09	0.001	−0.004	0.001	−0.018	−0.020	−0.002	−0.010	−0.064	−0.001
DR10	−0.001	0.042	0.000	−0.015	0.024	0.000	−0.007	−0.015	0.000
DR11	−0.012	−0.021	0.002	−0.030	−0.042	0.000	0.003	−0.064	0.001
DR12	0.009	0.066	0.004	−0.002	0.038	0.001	0.002	0.010	0.000
DR13	0.030	−0.004	0.005	−0.013	0.000	0.001	−0.009	−0.020	0.000
DR14	0.010	0.013	0.007	−0.052	0.035	0.003	−0.001	−0.002	0.001
DR15	0.019	0.010	0.003	−0.037	0.023	0.002	−0.030	0.006	−0.003
DR16	0.012	0.077	0.000	0.012	0.039	0.000	−0.003	0.031	0.001
RS01	0.031	0.119	0.017	0.034	0.087	0.006	0.064	−0.018	0.007
RS02	−0.001	0.031	0.001	−0.014	0.014	0.001	0.006	−0.021	0.002
RS03	−0.008	0.098	0.003	0.031	0.034	−0.001	−0.011	0.047	0.000
RS04	−0.033	0.027	−0.005	−0.010	−0.032	0.002	0.001	−0.046	0.000
RS05	−0.011	0.031	0.001	−0.012	−0.004	−0.002	−0.013	−0.007	−0.001
RS06	−0.017	−0.018	0.005	−0.015	−0.054	−0.001	−0.010	−0.009	0.000
RS07	−0.016	0.040	0.016	−0.022	−0.019	−0.002	−0.019	0.005	−0.001
RS10	0.007	0.087	0.005	0.005	0.023	−0.002	−0.023	0.008	0.000
RS15	0.000	0.038	0.011	−0.019	0.004	0.002	0.003	−0.010	0.003
RS16	0.003	0.043	0.004	0.007	−0.004	0.000	−0.001	−0.024	0.000
RS18	−0.011	0.023	0.003	0.015	−0.038	0.000	−0.010	−0.017	0.001
Median	0.002	0.031	0.003	−0.006	0.010	0.000	−0.002	−0.014	0.000
MAD	0.013	0.018	0.002	0.013	0.020	0.001	0.008	0.011	0.001

Supplementary Figures

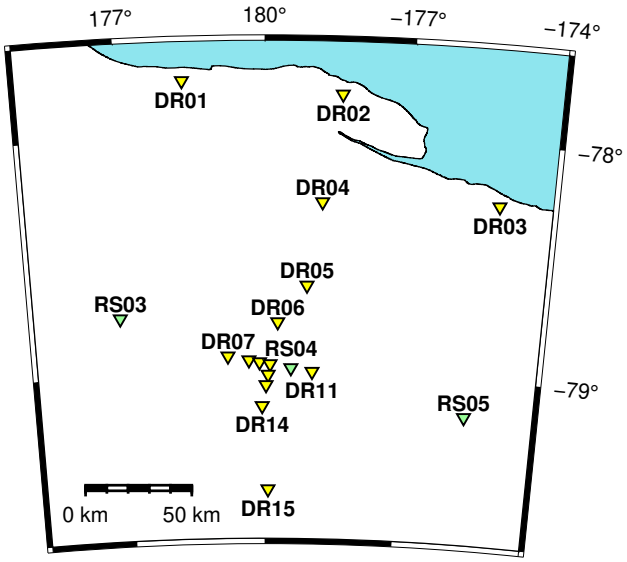

Fig. S1. Map of RIS/DRIS ice front stations. DR stations (yellow) sampled at 200 Hz; RS stations (green) sampled at 100 Hz, except for RS04 which was also 200 Hz. DR02 was sited on the semi-detached Nascent Iceberg.

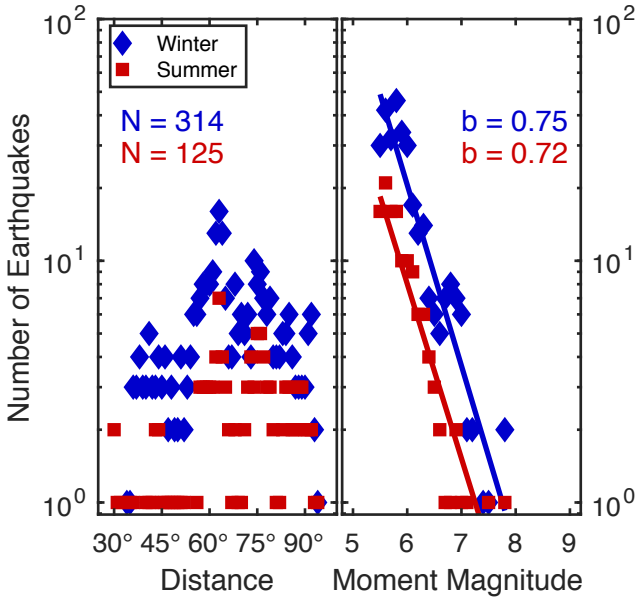

Fig. S2. Population metrics for all earthquakes used in this study. N-values indicate the number of earthquakes for Winter (blue) and Summer (red). b-values are the slopes of the Gutenberg-Richter relation, as determined with least squares regression. The P-wave analysis used all earthquakes shown here; the S- and surface wave analyses used the subsets defined in Table 1.

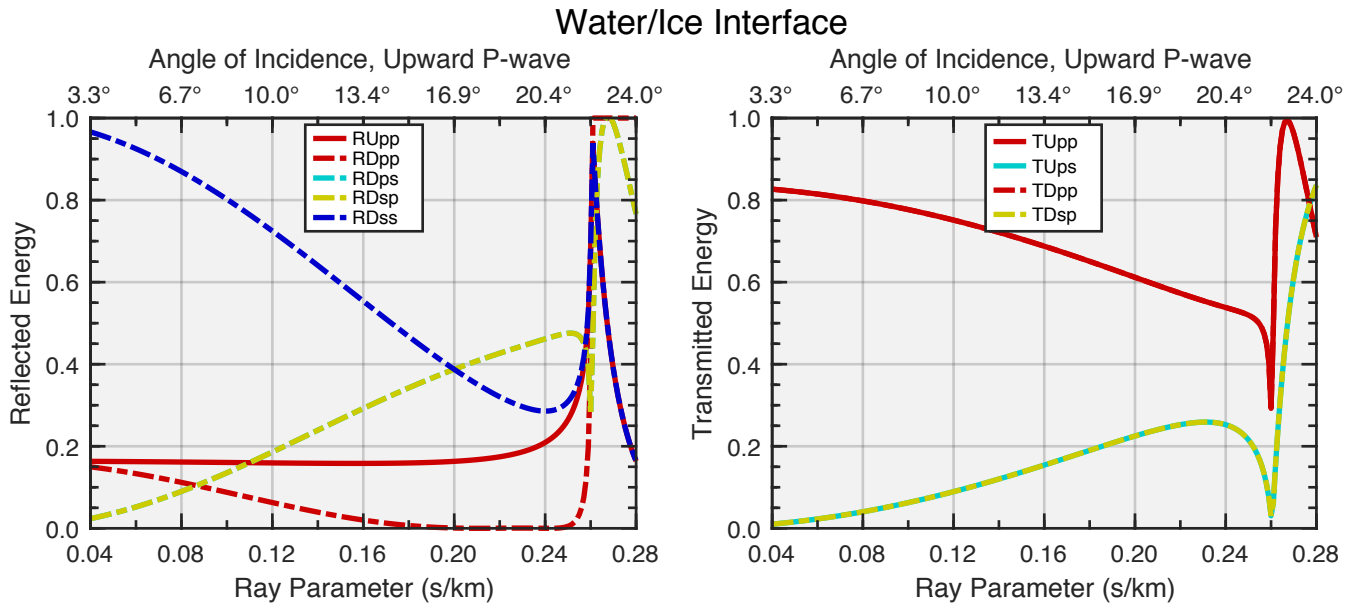

Fig. S3. Reflected and transmitted energy coefficients for the ice/water interface (Aki and Richards, 2002), using the values listed in Table 2. Coefficients read left-to-right; e.g., TDsp indicates the transmission coefficient for a downward propagating S-to-P conversion. RDps and RDsp overlap. TUpp and TDpp also overlap.

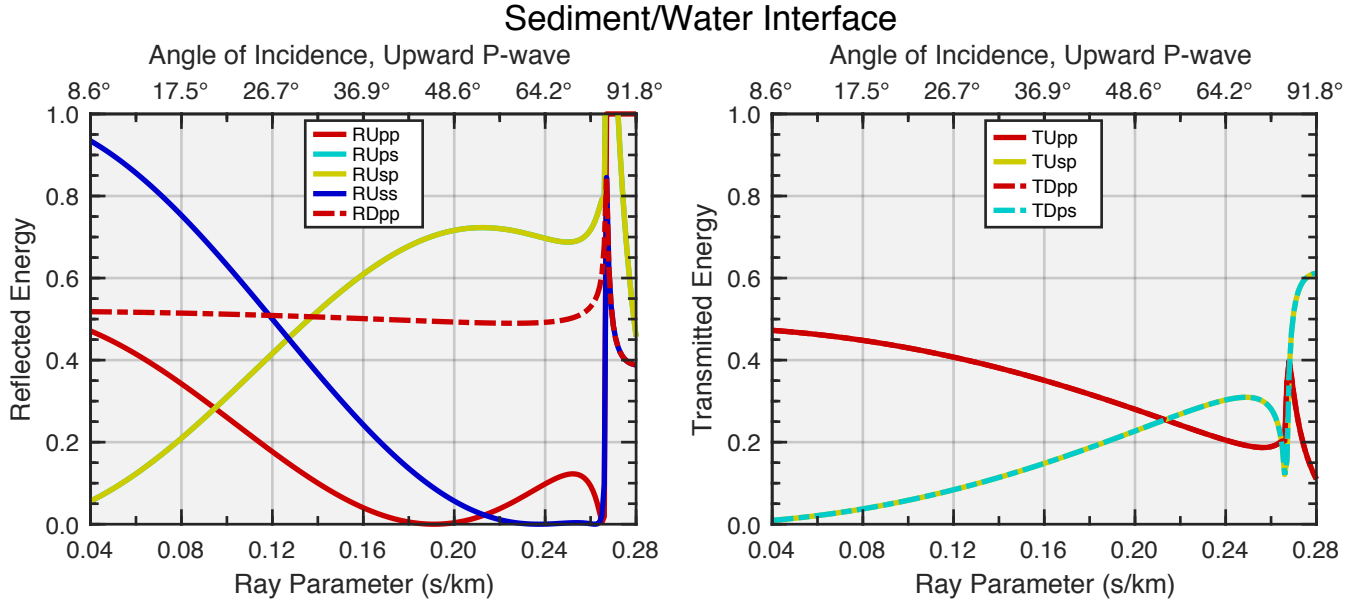

Fig. S4. Reflected and transmitted energy coefficients for the water/sediment interface (Aki and Richards, 2002), using the values listed in Table 2. Coefficients read left-to-right; e.g., TDps indicates the transmission coefficient for a downward propagating P-to-S conversion. RUps and RUsp overlap. TUpp and TDpp also overlap.

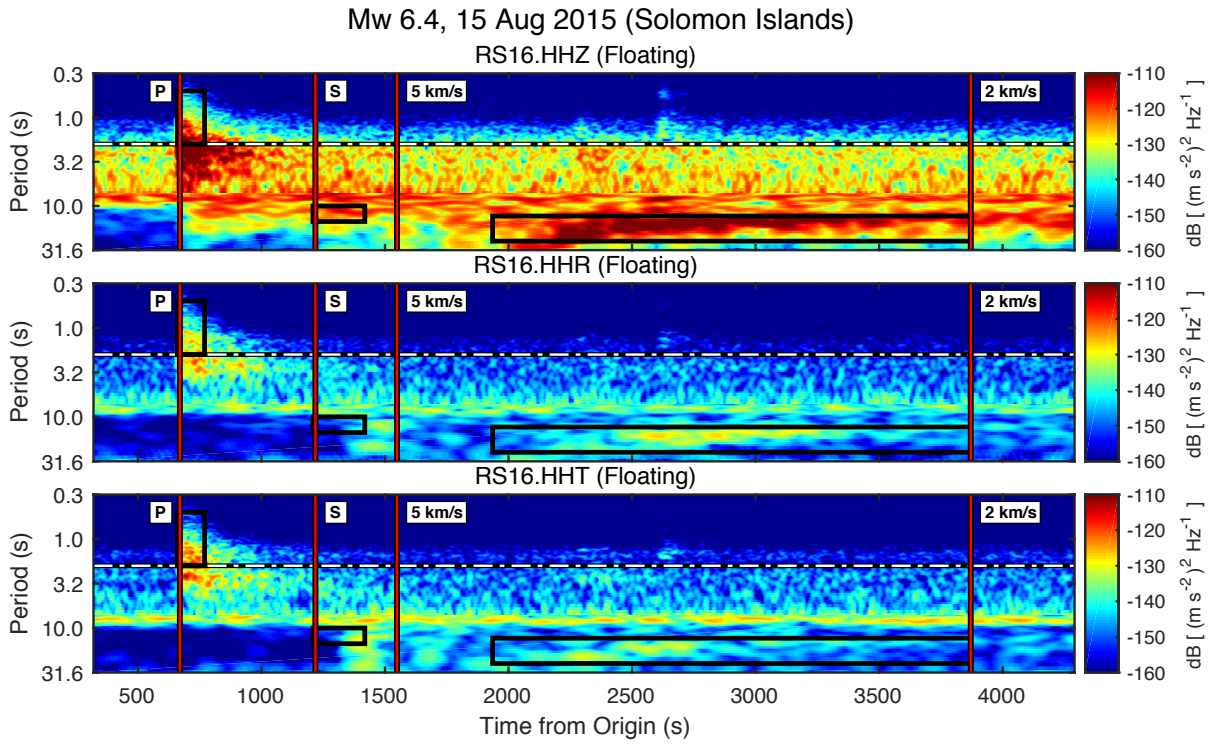

Fig. S5. Spectrogram without background normalization from floating station RS16 for the M_w 6.4 earthquake shown in Figure 3.

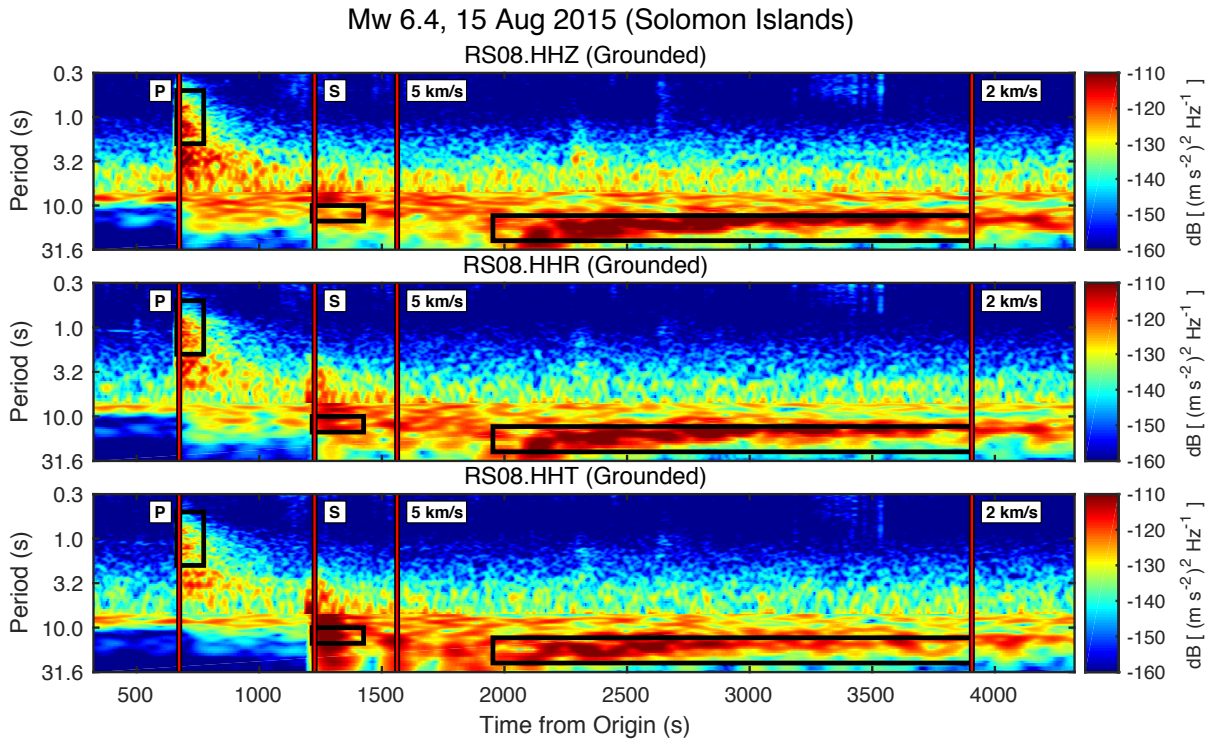

Fig. S6. Spectrogram without background normalization from grounded station RS08 for the M_w 6.4 earthquake shown in Figure 4.

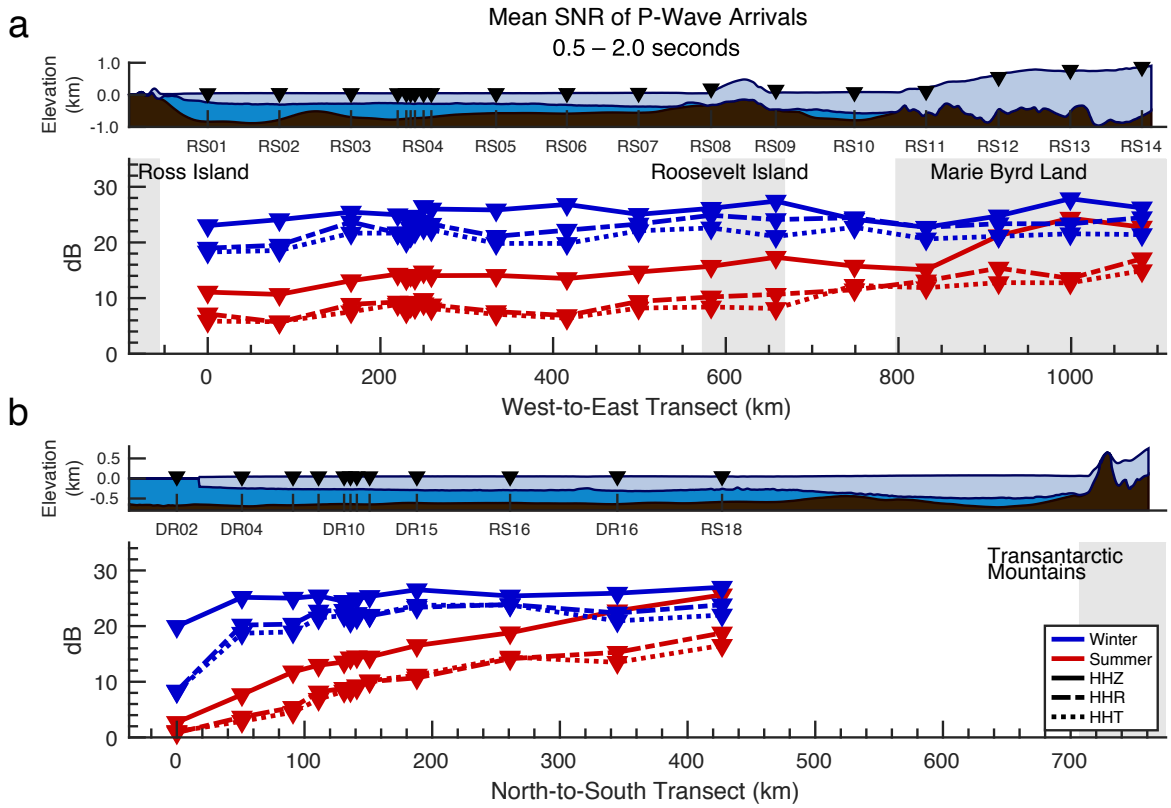

Fig. S7. Seasonal and geographic variations in average acceleration power for teleseismic P-wave arrivals, using data uncorrected with Equation 1. Compare to Figure 5.

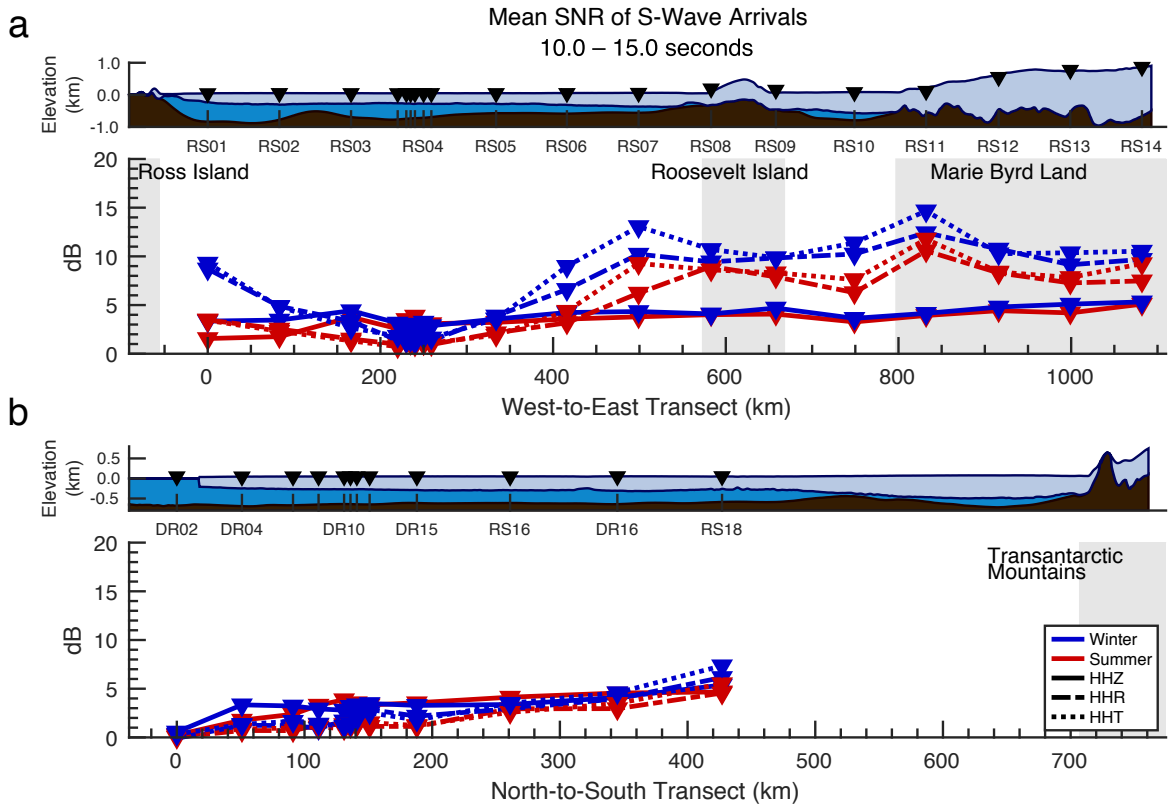

Fig. S8. Seasonal and geographic variations in average acceleration power for teleseismic S-wave arrivals, using data uncorrected with Equation 1. Compare to Figure 8.

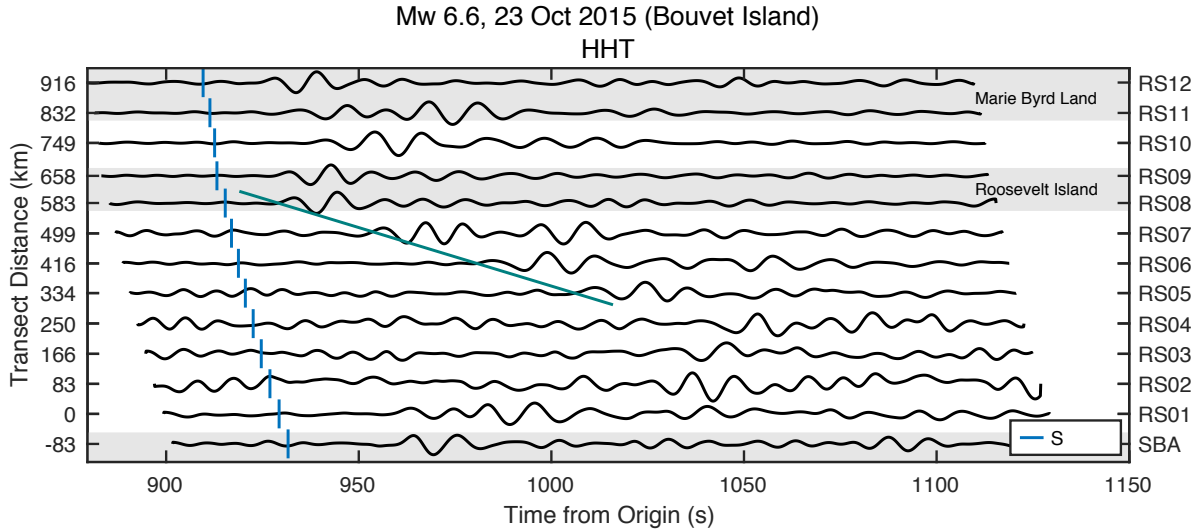

Fig. S9. Transverse component record section for teleseismic S-waves arriving from the 23 October 2016, M_w 6.6 Bouvet Island earthquake (hypocenter depth: 11 km). At RS08, the back azimuth for this event is -100° from the W-E transect great circle arc. The teal line marks the (manually fit) travel time curves for S_0 Lamb waves inferred to be generated by S_H-waves incident at the Roosevelt Island grounding line (Equation 7, $\varphi \approx 90°$). S_0 Lamb wave propagation velocity was 3.23 km s^{-1}. See Figure 9 for more details.

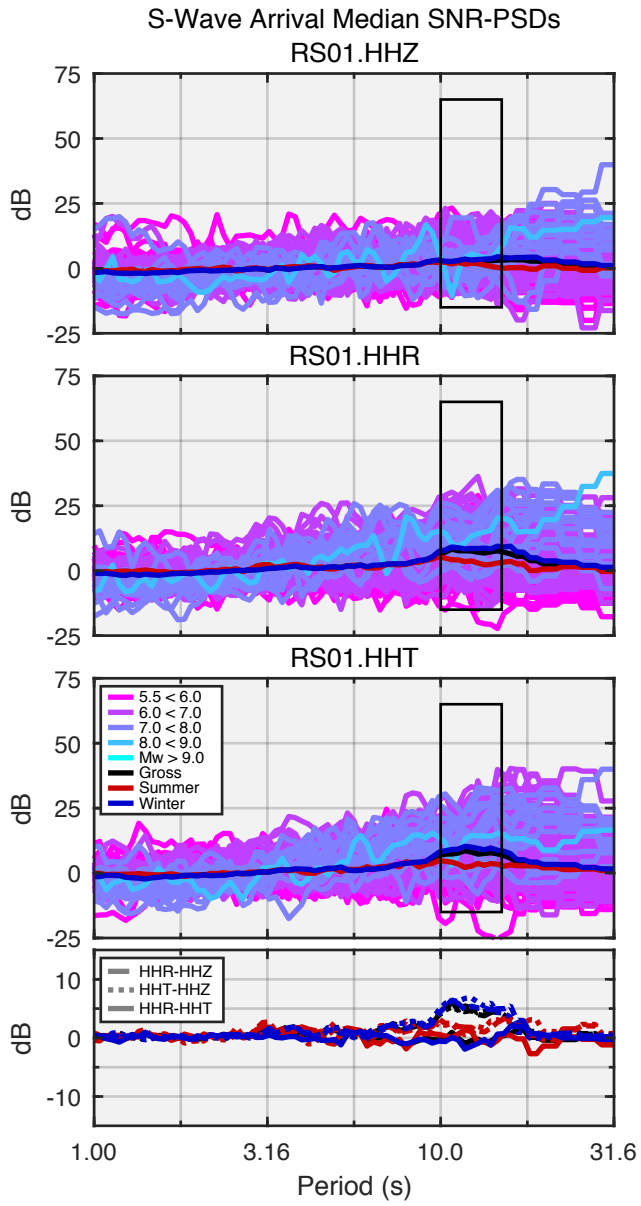

Fig. S10. Median SNR-PSDs for all teleseismic S-wave arrivals recorded at near-shelf-edge floating station RS01. The broad spectral peaks in the 10–15 s period band (black box) are horizontally polarized teleseism-induced S_0 Lamb waves. Theoretically, shear horizontal plate waves may also be excited by teleseismic S-wave arrivals and would also be observed in this band; at this time, we have not observed such a conversion.

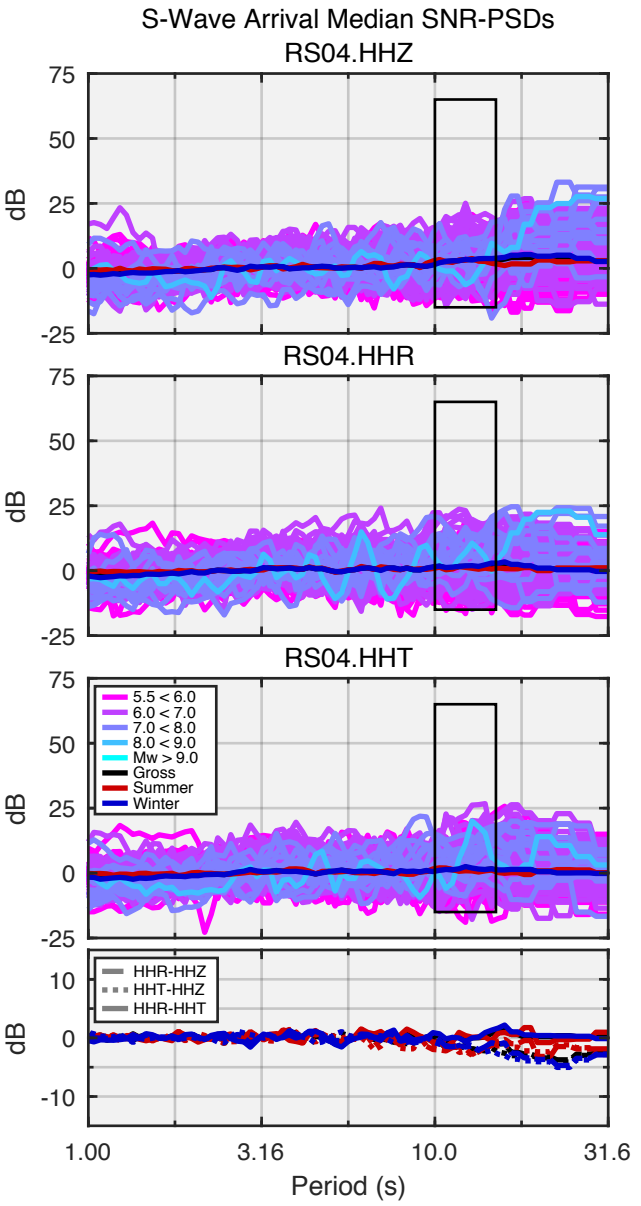

Fig. S11. Median SNR-PSDs for all teleseismic S-wave arrivals recorded at interior floating station RS04, ∼250 km from the nearest grounding line. Note the significant attenuation in horizontal plate wave energy (black box).

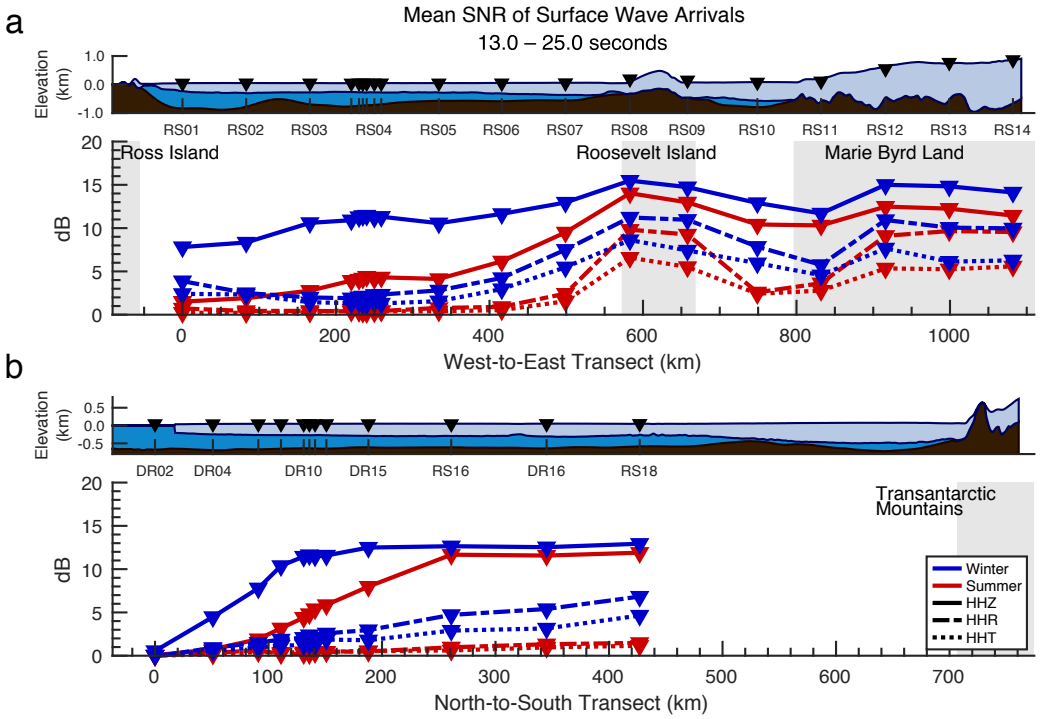

Fig. S12. Seasonal and geographic variations in average acceleration power for teleseismic surface wave arrivals, using data uncorrected with Equation 2. Compare to Figure 12.

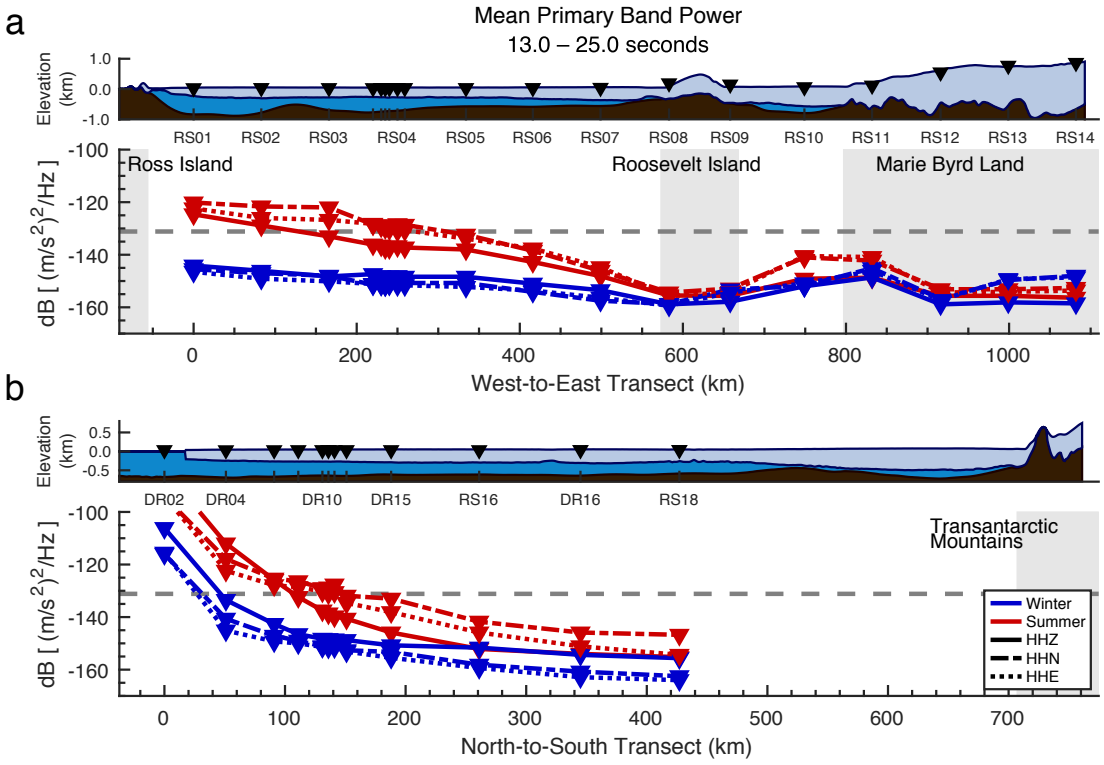

Fig. S13. Seasonal and geographic variations in average seismic acceleration power for ambient noise in the 13–25 s period band, adapted from the 10–20 s Primary band presented in Baker and others (2019). The dashed gray lines indicates the mean Global Seismic Network high-noise model limit for this period band.